JAAS

Journal of Analytical Atomic Spectrometry

rsc.li/jaas

ROYAL SOCIETY
OF CHEMISTRY
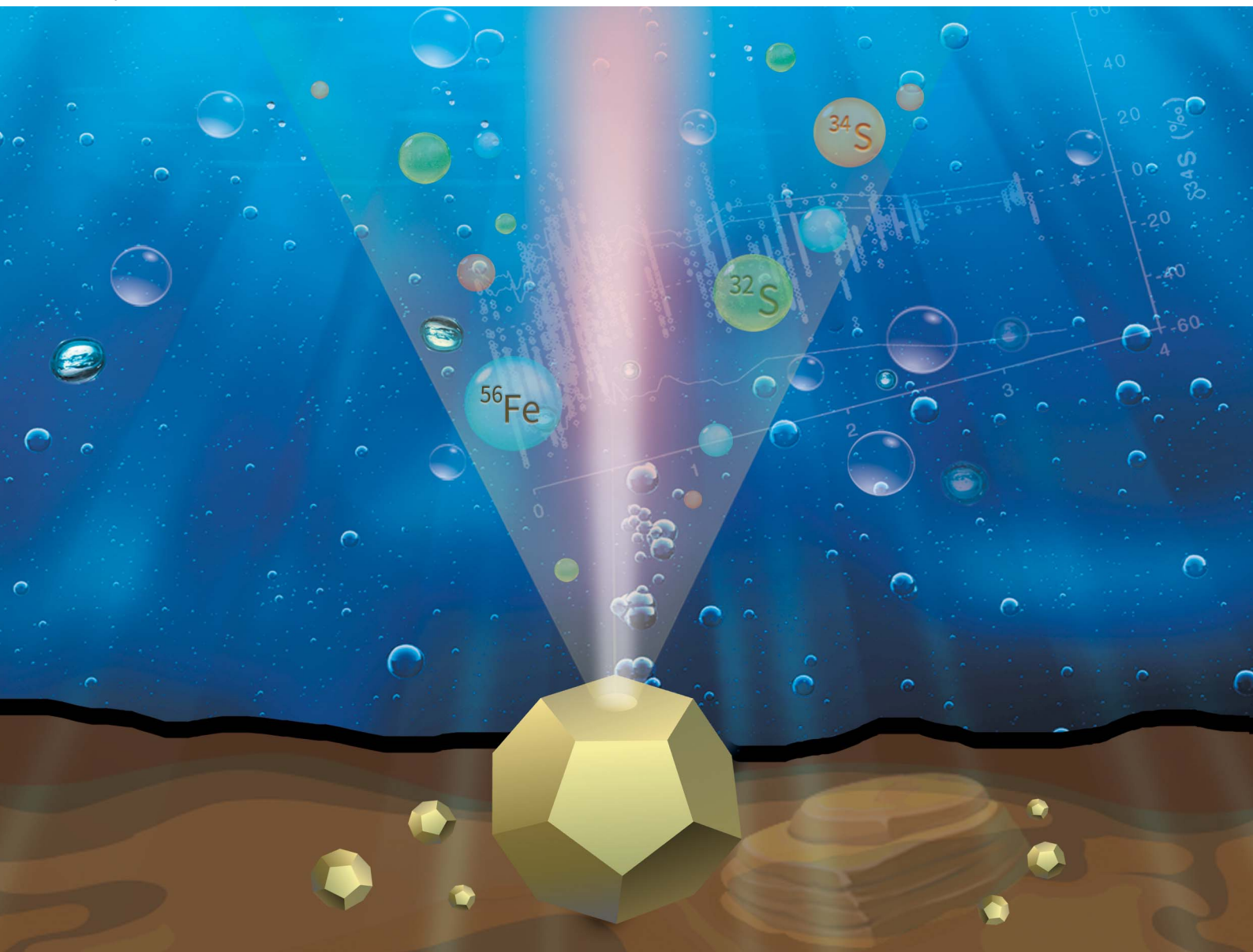
PAPER
Youwei Chen, Jianfeng Gao *et al.*
High spatial resolution and precision NanoSIMS for sulfur
isotope analysis

JAAS

Check for updates

High spatial resolution and precision NanoSIMS for sulfur isotope analysis†

Youwei Chen, [ID] * Zhuojun Xie, Shaohua Dong, Quanliang Lei and Jianfeng Gao*

Nano-scale secondary ion mass spectroscopy (NanoSIMS) is a powerful tool for determining the sulfur isotope composition of micrometer-sized minerals. However, the high spatial resolution of $\delta^{34}S$ analysis comes at the expense of accuracy, which limits the applicability of NanoSIMS to sulfur isotope analysis. The method proposed here couples high lateral resolution ($>1 \times 1 \mu m^2$) with high precision. A Faraday cup (FC, for ^{32}S)–electron multiplier (EM, for ^{34}S) detector combination is selected to improve static counting and mitigate the quasi-simultaneous arrival (QSA) effect. The instrument is set and tuned to achieve high transmission ($\sim$70%) and mass resolution power (MRP $\sim$ 5600 for ^{32}S). A primary beam of 3.5 pA was rastered on a scan area of $1 \times 1 \mu m^2$ to acquire the $\delta^{34}S$ isotope ratio. The $\delta^{34}S$ ratios of the four analyzed standard samples are consistent with previously reported values, with reproducibility (1 SD) better than 0.5‰. Because EM aging affects the accuracy of the sulfur analysis results, periodically adjusting the maximum value of the peak-height distribution (PHD_{max}) of the EM during the analysis is necessary. Careful optimization of the height (Z position) at different locations (samples) ensures precise and accurate $\delta^{34}S$ values. The S isotopic characteristics of framboidal pyrite from the Shuiyingdong Carlin-type Au deposit are determined using this method. The results indicate that the pyrite crystallite comprising framboidal pyrite is rimmed by ore pyrite, supporting the magmatic hydrothermal origin of the deposit. The developed method can be used for analyzing the $\delta^{34}S$ of pyrite samples with a limited analyzable region ($>1 \times 1 \mu m^2$) with high precision.

Introduction

Sulfur (S) bearing minerals are widely distributed in various geological bodies. Due to the large differences among the atomic masses and valence states of S, fractionation of sulfur isotopes in these minerals is significant, making the sulfur isotopic system an important tool for tracing sulfur reservoirs and constraining various geochemical processes.[1–4]

In recent years, the development and popularization of laser ablation inductively coupled plasma mass spectrometry (LA-ICP-MS) and secondary ion mass spectrometry (SIMS) micro-analysis techniques have enabled the *in situ* microanalysis of sulfur isotopes.[5–16] Compared to traditional bulk methods (IRMS, TIMS, and MC-ICPMS), *in situ* microanalysis is efficient and convenient and has micron-scale spatial resolution, which has a unique advantage in analyzing minerals with complex genesis or multi-phase superposition. Most *in situ* analyses of sulfur isotopes have been conducted using the CAMECA IMS f-series, large-geometry SIMS (LG-SIMS, CAMECA 1270/1280 or SHRIMP), and LA-MC-ICPMS instruments, which have a typical

lateral resolution of 10–60 μm. However, for samples with an analyzable region that is less than 5 μm in size with micron-scale zonings (including sulfides associated with hydrothermal activity and metamorphism, microbiota activity related minerals (framboidal pyrite), and planetary particles), only *in situ* sulfur isotope analysis with nano-scale secondary ion mass spectrometry can permit localized targeting.

NanoSIMS (CAMECA Nano 50 and Nano 50L), which is characterized by sub-micrometer lateral resolution, high transmission efficiency, and high sensitivity, has been widely used in cosmochemistry, bioscience, materials science, and geoscience.[17–21] It has been shown to be a powerful tool for determining the sulfur isotope content of micrometer minerals to solve a range of geological problems.[22–29]

Moreover, the spatial resolution and precision of sulfur isotope analysis with NanoSIMS have been greatly improving since NanoSIMS was first applied to test the S isotopic compositions of interplanetary dust particles.[11,25,30–33] Nishizawa *et al.* performed $\delta^{34}S$ analysis (1 SD = 1.6‰) for pyrite with a scan area of $1.5 \times 1.5 \mu m^2$.[32] Zhang *et al.* reduced the lateral resolution for $\delta^{34}S$ analysis for pyrite (1 SD = 1.5‰) down to a scan area of $0.5 \times 0.5 \mu m^2$.[31] Although the $\delta^{34}S$ analysis spatial resolution was improved, its precision remained very poor (1 SD > 1.5‰), which limited the application of NanoSIMS in sulfur

State Key Laboratory of Ore Deposit Geochemistry, Institute of Geochemistry, Chinese Academy of Sciences, Guiyang, 550081, People's Republic of China. E-mail: chenyouwei@mail.gyig.ac.cn; gaojianfeng@mail.gyig.ac.cn

This journal is © The Royal Society of Chemistry 2022

J. Anal. At. Spectrom., 2022, **37**, 2529–2536 | **2529**

isotope analysis. Therefore, a method with high resolution and precision for S isotope analysis is urgently required.

In this study, we introduce a method and setting to improve the lateral resolution (a square side of 1 μm) for NanoSIMS δ^{34}S analysis with high precision and accuracy. Two factors—EM aging and height influence—that affect the accuracy of sulfur isotope measurement are examined. Subsequently, the developed method is applied to measure the δ^{34}S ratios of the framboidal pyrite from the Shuiyingdong Carlin-type gold deposit to constrain the formation of the deposit. This method can be used for analyzing the δ^{34}S of samples with a limited analyzable region (>1 × 1 μm^2) with high precision and accuracy.

Sample description and preparation

The sulfur isotopic analyses in this study were conducted on the CAMECA NanoSIMS 50L instrument (installed in June 2021) at the State Key Laboratory of Ore Deposit Geochemistry (SKLODG), Chinese Academy of Sciences, Guiyang, China (Fig. 1).

Four pyrite samples including Balmat, Ruttan, Py1117, and SRZK were examined in this study. The Balmat and Ruttan pyrite grains were supplied by Dr Bin Fu from the Australian National University, Canberra, Australia. The Ruttan pyrite was obtained from deposits located at Leaf Rapid, Canada, which is hosted in metamorphous Aphebian-age Wasekwan Group rocks.[34] The Balmat pyrite was obtained from deposits hosted in Grenville-age marbles from the Adirondack Mountains, New York. The δ^{34}S values of both the Balmat and Ruttan pyrites were analyzed using conventional methods (15.1 ± 0.2‰ for Balmat, and 1.2 ± 0.1‰ for Ruttan).[34]

Py1117 and SRZK pyrite grains were supplied by Dr Yang Wei from the Institute of Geology and Geophysics, Chinese Academy of Sciences, Beijing, China. PY-1117 was obtained from pyrite veins in the Qulong porphyry copper deposit, China. Detailed information of the SRZK pyrite is unavailable. Py1117 and SRZK pyrite were also measured using conventional δ^{34}S methods (0.3 ± 0.1‰ for Py1117, and 3.6 ± 0.1‰ for SRZK).[31,35]
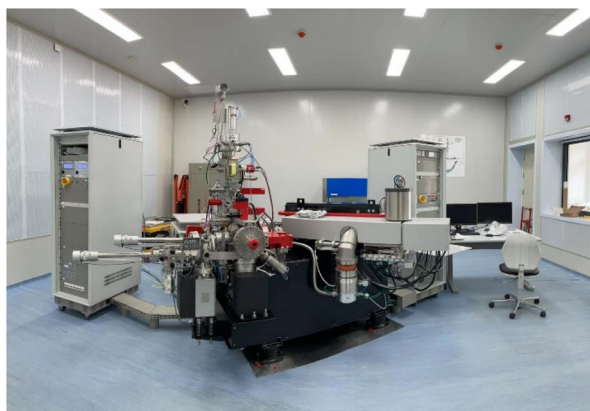
All the pyrite grain samples (ranging from 100 to 500 μm in size) were embedded in epoxy resin and combined into polished disks with a diameter of 10 mm (Fig. 2b).

The ore sample (SYD-3A-1) was collected from the 3A ore body in the Shuiyingdong Carlin-type gold deposit, China. Most of the pyrite grains in this sample had a core-rime texture, whereas few framboidal pyrite grains exhibited heterogeneity at the microscale, which would be ideal for this study. A 10 mm disk of the thin-section was cut by using a wire-cutting machine.

The pyrite and thin-section disks were then coated with gold (~20 nm thick) and mounted in a 10 mm biology-type sample holder (Fig. 2a).

Experimental

Spatial resolution and analysis precision are important but negotiable qualities in microanalysis. Spatial resolution determines the minimum size of the analysis area, but the sampling quantity of the analyte limits the counting statistics of secondary ions and the analysis precision (accuracy and reproducibility). As the spatial resolution improves, the sampling size is reduced, and the counting statistics decrease, which lowers the precision of the isotope ratio analysis. Hence, the improvement in the spatial resolution is largely at the cost of analytical precision.[36] In the NanoSIMS region, the primary beam is usually rastered on the sample surface instead of statically focusing the beam to sputter a steep-sided crater and induce the depth effect.[37,38] Therefore, the spatial resolution of the isotope analysis, equated with the analysis area (scan area of the primary beam), is largely based on the primary beam current. A high primary current leads to a high secondary ion rate (counts per second), but a large raster size to stabilize the secondary ion beam (SIB) (sputter in the steady state sputtering regime).[39]

The first method reduces the raster size by reducing the primary beam current to increase the spatial resolution of NanoSIMS. This also lowers the precision of isotopic measurements because of the reduced material sputtering.[40] Therefore, the key is to find a good balance between the primary beam, the analysis area, and counting statistics to ensure high spatial resolution and a high-precision result.

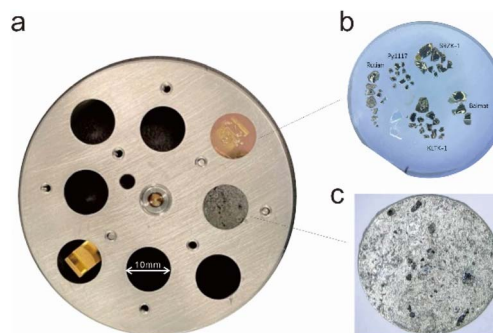Fig. 1 Photographic image of NanoSIMS 50L in SKLODG, China.

Fig. 2 (a) Samples placed in a 10 mm biology-type holder. (b) Image of the four types of standard pyrite grains examined in the study. (c) Sample from the Shuiyingdong Au deposit.

Instrument setting

Two types of detectors are available for NanoSIMS 50L: FC and EM for high and low signals, respectively. Several detector combinations can be used based on the required spatial resolution and precision. For high-resolution requirements, two detector combinations are typically used: FC (for ^{32}S)–EM (for ^{34}S) and EM–EM.[31]

Although EM–EM detector combinations can theoretically achieve higher spatial resolution owing to the use of a weak-current primary beam, they have many drawbacks. Firstly, the precision of the sulfur analysis by the EM–EM combination is low because of the upper limit of the count rate for the EM (<2 × 10^6 cps). Studies showed that the ultimate precision of multiple ion counters is of the order of 1‰, given their count rates and dead time on individual counters.[41,42] This situation was also documented in a study with an EM–EM combination (1 SD = 1.5‰ for δ^{34}S).[31,32] Secondly, the QSA effect,[43] EM aging,[44] and dead time correction are highly problematic because the abundance of ^{32}S is much higher than that of ^{34}S (over 20 times). QSA effects create large mass-independent inaccuracies during isotope measurements.[45] The speed of EM aging for ^{32}S is much faster and critical, complicating adjustments for EM aging and the correction of instrumental mass fractionation (IMF). Further, the dead time correction in the EM–EM combination is obviously different and should also be monitored and corrected carefully owing to the large difference in the intensities of the ^{32}S and ^{34}S beams.[40]

The FC detector is stable and undetectable drift sensitivity occurs within a period of analysis. More importantly, the FC detector can measure a much higher ion current (>2 × 10^6 cps) without any influence of QSA and aging, which is crucial for high precision isotope analysis. The use of an FC–EM detector combination enables signals in the optimal range of both isotopes (signals of several million cps for ^{32}S on the FC detector, and hundreds of thousands of cps for ^{34}S on the EM detector) to be detected, thereby matching with the differences in the abundance of ^{32}S and ^{34}S. Therefore, the FC–EM detector combination is preferred in this study because it permits high spatial resolution and greater precision.

To maximize the use of secondary ion signals, the transmission of the SIB should be tuned very high. However, the peak shape of the SIB in the detector should also be considered (Fig. 3a). A high transmission (~70% of the maximum, compared with all the slit openings) with sufficiently flat SIB peaks is achieved using ~180 μm width of the entrance slit (ES), ~100 μm width of the exit slit (EnS) and an open aperture slit (AS). Under these conditions, the mass resolving power (MRP) is ~5600 for ^{32}S ($M/\Delta M$, CAMECA definition related to the peak width between 10% and 90% intensity) (Fig. 3a), which is sufficient to distinguish isobaric interferences for masses ~32 (^{32}S$^-$, ^{16}O$_2{}^-$) and ~34 (^{34}S$^-$, ^{33}SH, ^{16}O^{18}O$^-$). The NMR field sensor is used during the analysis to lock the magnetic field with high precision.

The intensity of the primary beam is largely determined by the required precision. For isotope ratio measurements, the level of precision required is largely determined by the number of counts recorded on the least abundant isotope (^{34}S$^-$ in this study).[37] Calculations show that a Poisson uncertainty of δ^{34}S (1 SE) within 0.2‰ can be achieved, when accumulated ^{34}S$^-$ counts are >2.5 × 10^7 counts, and corresponding ^{32}S$^-$ accumulated counts reach >5.5 × 10^8 counts. If the acquisition time is ~150 s, the signal intensity of ^{32}S$^-$ should be higher than 3.7 × 10^6 cps. Previous studies showed that the yield of ^{32}S$^-$ in pyrite is 1–1.3 × 10^9 cps nA^{-1} with SIMS.[12,14,31,46] Therefore, a primary beam of ~3.5 pA is chosen for raster scanning under this instrument setting.

Analysis setting

After appropriate instrument setting and tuning, a primary beam of 3.5 pA with an impact energy of 16 keV was rastered on a sample with a different area to obtain a sufficiently wide and constant SIB (acquisition time > 200 s, including a data collecting time of ~150 s and SIB auto-centering time of ~50 s) (Fig. 3b). The constant secondary signal (in the steady state regime) with a scan area of 0.5 × 0.5 μm^2 is too narrow (<100 s), and the signal dramatically increases after the interval of constant intensity, which lowers the precision and accuracy. The secondary signal obtained by using a scan area of 1 × 1 μm^2 remains constant over a ~200 s interval, and the signal increases slowly after the interval (with little effect on the precision). Therefore, a scan area of 1 × 1 μm^2 is applied for acquiring the SIB in this study.

Before each analysis, the sample surface was pre-sputtered (3.5 pA) for 100 s to remove the gold coating and possible contaminations, followed by a SIB auto-centering process. Both the ^{32}S$^-$ and ^{34}S$^-$ ions were measured for 300 cycles, with each cycle being of 0.54 s duration. The total analysis time, including pre-sputtering, was ~6 min per measurement.

The baseline drift of the FC detector affects the stability of the isotope analysis. The baseline of the FC was measured for 10 s before and after each analysis. On the NS50L, the background noise of an FC with a resistance of 10^{11} Ω is given as 5 × 10^{-16} A, measured over 5 s. The equivalent count rate of the FC background noise is ~3100 c s^{-1} which was recorded over 10 min with an integration time of 5 s. The dead time on the EM is set to 44 ns based on the instrumental design. The raw results are given with the EM dead time correction and FC baseline correction for individual analyses. All these corrections were applied using the CAMECA software.
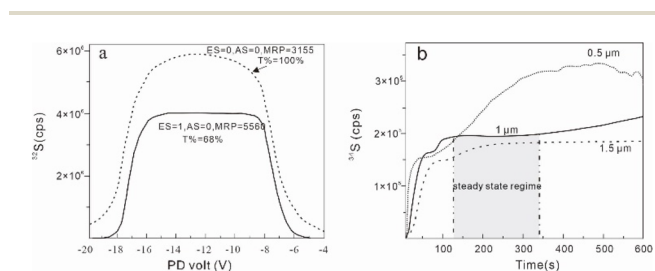

Fig. 3 (a) MRP shape of ^{34}S and transmission with different ES settings. (b) ^{34}S signal vs. time diagram with a different primary beam and scan area.

In this study, the measured $^{34}S/^{32}S$ ratios were normalized using Vienna-Canyon Diablo Troilite (V-CDT) standard compositions $(^{34}S/^{32}S_{V-CDT} = 0.0441626)$[47] as $\delta^{34}S_{raw}$ (‰) $= [\{(^{34}S/^{32}S_{sample})/(^{34}S/^{32}S_{v-CDT})\} - 1] \times 1000$. The IMF factor was calculated for each analysis from the relation IMF $= \delta^{34}S_{true} - \delta^{34}S_{RAW}$. Then, the IMF was used to calculate the $\delta^{34}S_{cor}$ of the unknown sample from the relation $\delta^{34}S_{cor} = {}^{34}S_{RAW} + IMF$. The $\delta^{34}S$ result was reported with the associated analytical uncertainty (SE) and standard deviation (SD), which was estimated as the square sum of the standard deviation of the measurement and the uncertainty of the IMF of the reference sample (Balmat in this study). The uncertainty in the recommended value for the reference pyrite was not included.

Results

Table 1 summarizes the results of the sulfur isotopes ($\delta^{34}S$) of the analyzed pyrites in this study. More detailed information and raw data are included in ESI Table S1.†

The typical secondary ion current of $^{32}S^-$ is ~4.3 × 10⁶ cps for pyrite with a primary beam of ~3.5 pA in the study. This indicates that the yield of $^{32}S^-$ is ~1.2 × 10⁹ cps nA⁻¹, which is consistent with that of other studies on CAMECA 1280 and NanoSIMS.[12,14,31,46]

According to Poisson's statistical theory, the internal precision isotope measurement mainly depends on the signal statistics and would be affected by the signal stability.[5] The typical total count of $^{34}S^-$ in this study is ~3 × 10⁷, indicating Poisson uncertainty (RSE) of ~0.2‰. The analytical uncertainties (RSE) in this study are smaller than 0.3‰ for $\delta^{34}S$, which is close to the Poisson uncertainty, indicating that the signal is sufficiently stable. The RSE also indicates that the signal-to-noise ratio and the drift of the ratio (caused by the depth effect) have a lesser effect on the precision and accuracy.

External reproducibility of Balmat pyrite in $\delta^{34}S$ was between 0.3 and 0.5‰ (1 SD) (Fig. 4). The grain-to-grain test was carried out on the four pyrite samples. All the external reproducibility values of these pyrites were between 0.3 and 0.5‰ (1 SD). The Balmat pyrite was treated as the reference standard to calculate the IMF factor and the $\delta^{34}S$ ratio of the other pyrite samples. The $\delta^{34}S$ values of all pyrite samples are consistent with the
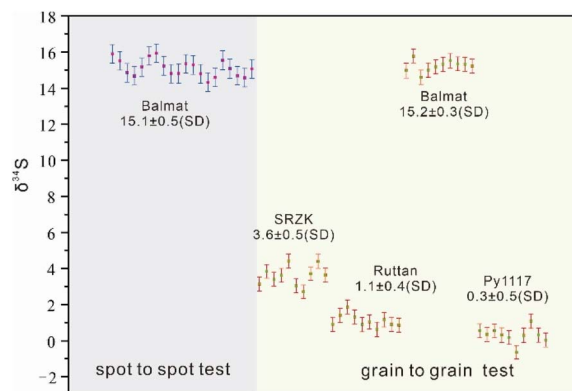

Fig. 4 Analysis of $\delta^{34}S$ of the four pyrite standards in this study.

recommended values within analytical uncertainties, proving the accuracy of this sulfur isotope analysis method.

In summary, the result shows that the method tested here for sulfur isotope analyses to determine $\delta^{34}S$ has high spatial resolution (a square side of 1 μm), high precision (higher than 0.5‰), and high reliability.

Challenges of high resolution sulfur analysis with NanoSIMS

Many factors can affect the accuracy and precision of sulfur isotope measurements, including the surface topography of samples, a lack of matrix-matched standards or compositional heterogeneity, stability of the magnetic field, and FC background noise.[11–14,31,48,49] Two main factors affect the accuracy of the sulfur isotope ratio when conducting high-resolution sulfur analysis with NanoSIMS: EM aging and height (Z) influence.

EM aging

EM aging occurs with increasing cumulative counts owing to the deposition of carbon on the last dynode, which decreases the gain efficiency of the EM detector, and ultimately reduces ion counting.[44] The EM aging can be recorded by noting the reduction in PHD_{max} of the EM detectors in NanoSIMS.

For sulfur analysis with the FC–EM detector combination, EM aging decreases the ^{34}S counts and $^{34}S/^{32}S$ ratios. Therefore, it is important to evaluate the effect of EM aging on the $^{34}S/^{32}S$ ratio. We tested the $\delta^{34}S$ value under different PHD_{max} to demonstrate the effect of EM aging on the measured $\delta^{34}S$ value

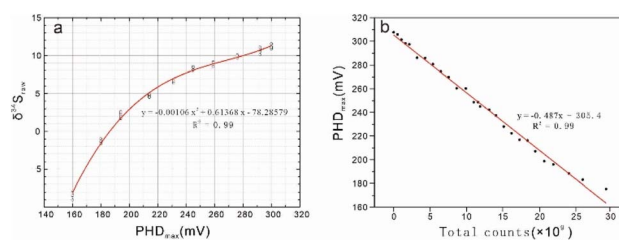**Table 1** NanoSIMS analyses of sulfur isotopes ($\delta^{34}S$) in sulfide standards and samples[a]

Sample	n	$\delta^{34}S_{RAW}$	RSE (‰)	IMF	$\delta^{34}S_{cor} \pm$ (SD)	$\delta^{34}S_{true} \pm$ (SD)
Spot to spot test						
Balmat	20	6.8	0.3	8.3	15.1 ± 0.5	15.1 ± 0.2
Grain to grain test						
Balmat	10	7.5	0.3	7.6	15.1 ± 0.5	15.1 ± 0.2
Ruttan	10	−6.5	0.3		1.2 ± 0.4	1.2 ± 0.1
Py1117	10	−7.3	0.2		0.3 ± 0.4	0.3 ± 0.1
SRZK	10	−4.0	0.2		3.5 ± 0.5	3.6 ± 0.1

[a] Here $\delta^{34}S_{cor}$ values are the data calibrated using the Balmat sample as the standard. The $\delta^{34}S_{true}$ values are the recommended values from ref. 30, 33 and 34.

Fig. 5 (a) $\delta^{34}S_{raw}$ value of Balmat pyrite as a function of EM PHD_{max} to demonstrate the effect of EM aging. (b) Variation in EM PHD_{max} with total counts.

2532 | J. Anal. At. Spectrom., 2022, **37**, 2529–2536

This journal is © The Royal Society of Chemistry 2022

(Fig. 5a). In this test, PHD_{max} changes by the adjustment of the EM voltage. When PHD_{max} is below 230 mV, the isotope ratio changes significantly ($\Delta\delta^{34}S > 0.5\permil/5$ V), whereas when PHD_{max} is above 240 mV, the influence on the isotope is relatively small ($\Delta\delta^{34}S < 0.5\permil/5$ V). Therefore, the recommendation is to set PHD_{max} of the EM above 240 mV for isotope ratio analysis.

EM aging can be countered by raising the high voltage (HV) of the EM. EM aging is commonly assumed to be proportional to the ion counts received by the EM detector.[50] In particular, in the case of an EM detector used to measure ions with a count rate higher than a few hundred thousand counts per second (cps), the rate of EM deterioration becomes critical. Therefore, the ion counts determine the required frequency and the increment of the EM HV adjustment to counter EM aging (stabilizing PHD_{max}). We evaluated the relationship between EM aging (PHD_{max}) and the total counts (Fig. 5b). In this test, the SIB was maintained at 3×10^5 cps and the EM PHD_{max} was checked periodically. The test showed that PHD_{max} typically varies linearly with time, and decays at a rate of 5.3 mV per hour, which is equal to 2×10^8 counts per PHD_{max} mV (Fig. 5b). This is slower than 2.6×10^8 counts per mV (calculated from Zhang et al.[31]). We concluded that the rate of EM deterioration may also relate to the EM HV (1890 V in this study). Therefore, we recommend periodically checking and adjusting the PHD_{max} based on the total counts and EM HV to control the accuracy of the S isotope test.

Height effect

The CAMECA NanoSIMS 50L is designed to work with the distance between the immersion lens and the sample surface set to 400 μm to obtain an intense smaller probe diameter. Therefore, the SIB is more sensitive to any change in the distance compared to the LG-SIMS. The distance (as the working distance) between the sample surface and lens has a significant effect on the reproducibility of the signal intensity and isotope ratio (Fig. 6). However, this distance always changes from sample to sample and point to point because of the surface roughness of the sample and the imbalanced loading in the sample holder. In NanoSIMS, the electrode EOS is used to compensate for the different heights of the sample (Z position) and focuses the SIB in the ES. However, any change in EOS results in a change in the focusing of the mass spectrometer secondary beam, which shifts the isotope ratio.[11]

To test the influence of EOS and the sample height on the S isotope analysis, we conducted two tests on Balmat pyrite: (1) changing the Z of the sample (step = 100 bit, equivalent to a difference in sample height of 17 μm) with SIB auto-centering (by scanning of the EOS and its related parameter values); (2) changing the Z of the sample (step = 100 bit) without SIB auto-centering (keeping the EOS constant). In test one (Fig. 7a), the $\delta^{34}S_{raw}$ values are roughly linear with Z and EOS. Further, increasing Z by 100 bits (equal to 17 μm for a real sample) slightly decreases $\delta^{34}S$ (~0.15‰), whereas EOS changes significantly with Z (100 bit change of Z is equal to 140 bit of EOS). In the second test (Fig. 7b), $\delta^{34}S_{raw}$ and the signal change significantly with Z without SIB auto-centering, indicating that the IMF of $\delta^{34}S$ is altered significantly.

It is noted that when Z varies considerably (>200 bit) across different positions, usually for transitions between standard and sample positions, SIB auto-centering cannot determine the optimal parameters, which significantly changes the secondary ion signal and $\delta^{34}S$, as demonstrated by test 2. Moreover, this variation will extend the time of the SIB auto-centering process, causing the sputtering of the SIB out of the steady state regime, which shifts both the SIB and $^{34}S/^{32}S$ ratio.

Therefore, carefully checking and optimizing the height (Z position) in different positions (samples) to stabilize EOS is key to obtain precise and accurate $\delta^{34}S$ results. However, the NanoSIMS does not allow one to view an optical image of the sample surface in the analysis position because of the short working distance between the sample and the immersion lens. Instead, the sample is first viewed in reflected light by a CCD camera in a remote position to locate the region of interest (ROI), and then translated back to the analysis position.[51] Therefore, it is very difficult to optimize the height of the samples during the analysis. In practice, it is recommended to (1) adjust the Z of the sample in the CCD position to obtain a focused image, (2) sputter the samples in the analysis position and obtain close EOS values (<100 bit) by adjusting the Z positions for different samples.

Applications

In situ NanoSIMS analysis with high precision and accuracy for measuring the ratio of sulfur isotopes in microminerals traces the source of framboidal pyrite in giant Shuiyindong Carlin-type Au deposits.
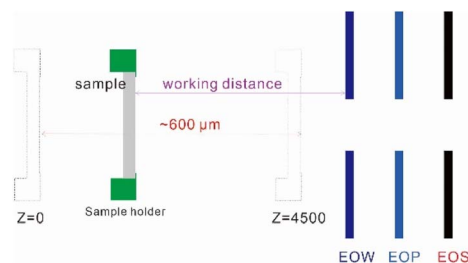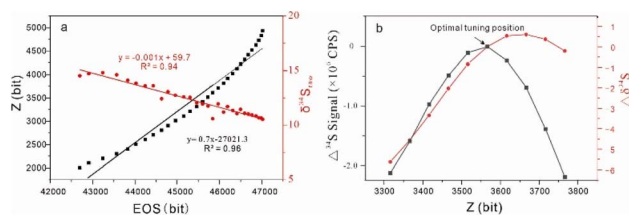

Fig. 6   Schematic of the coaxial column in NanoSIMS (modified from the NanoSIMS 50L user guide, CAMECA). Note that the working distance may vary due to different sample surface heights.

Fig. 7   (a) Effect of sample height (Z) on the EOS and $\delta^{34}S_{raw}$. (b) Effect of sample height (Z) on the ^{34}S signal and $\delta^{34}S_{raw}$ with the EOS held constant.

Geological background and results

The Shuiyindong Carlin-type Au deposit is the largest sediment-hosted Au deposit discovered to date in the Youjiang Basin. The deposit is controlled by the Huijiabao anticline and is a strata-bound Au deposit. The orebodies are mainly hosted by the bioclastic limestone of the upper Permian Longtan formation, and the strata above and below the bioclastic orebodies are typically thick-bedded argillite. Gold is principally incorporated in the arsenian pyrite as invisible Au.[52,53]

Pyrite is the main gold-bearing mineral in the deposit, commonly exhibiting core-rim zonation or occurring as fine-grained crystals. In addition, minor framboid pyrite is also present in ore minerals (Fig. 8a and b). Many studies have been carried out on the S isotopic compositions of the core-rim zonation by LA-MC-ICPMS and SHRIMP (Fig. 8c).[53] Owing to their small size, the S isotopic compositions of framboidal pyrites are difficult to analyze using LA-MC-ICPMS or LG-SIMS. To understand the sulfur isotope characteristics and genetic mechanism of the framboidal pyrite, the S isotopic compositions of this mineral were determined with the NanoSIMS method developed in this study.

The studied sample (SYD-3A-1) was collected from the 3A ore body in the deposit (Fig. 8a). Most of the pyrite grains in this sample exhibited a core-rime texture, with few framboidal pyrite grains occurring near the core-rim zonation pyrite. The BSE map shows that the framboidal pyrite grains are also characterized by the rim-core texture (Fig. 8b). The rim and core parts of the framboidal pyrite were chosen for S isotopic ratio analysis.
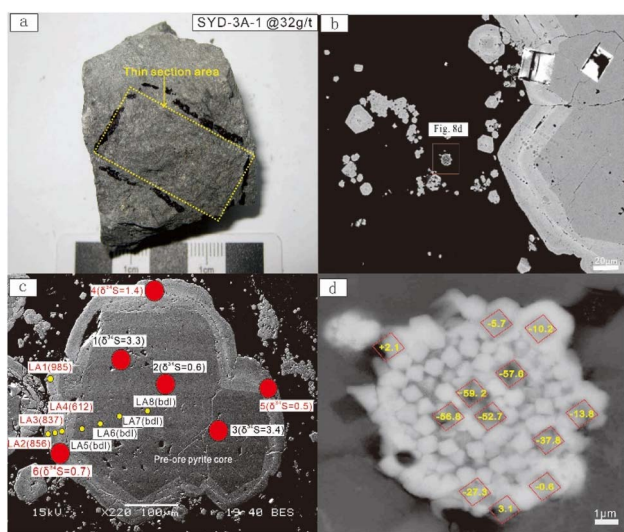

Fig. 8 (a) Photographic and (b) BSE image of the studied sample. Most of the pyrite grains in this sample exhibited a core-rime texture, while few framboidal pyrite grains occur near the core-rim zonation pyrite. (c) Anhedral pre-ore pyrite 2 is rimmed by ore pyrite. The yellow and red dots indicate locations of LA-ICP-MS and LA-MC-ICP-MS analyses, respectively, and are labeled with the analysis number and Au concentration in ppm and the δ^{34}S isotope composition in ‰, respectively (modified from Xie *et al.*[53]). (d) BSE image of the studied framboidal pyrite. The red squares indicate the location of NanoSIMS analyses and are labeled with the δ^{34}S isotope composition in ‰.

The results (ESI Table S2†) show that the core and rim areas of the framboidal pyrite have S isotopic compositions ranging from −59.2‰ to −52.7‰ and −37.8‰ to +2.1‰, respectively (Fig. 8d). The S isotopic characteristics of the rim area are significantly higher than those of the core area, and consistent with those of the core-rim zonation pyrite (δ^{34}S $\sim$ −3‰ to 3‰) (Fig. 8c).[53] The previous study showed that the pyrite rim contains high levels of Au and As, distinguishing it from the pyrite core and that it was precipitated during the ore stage (Fig. 8c).[53] The tiny pyrite crystallites comprising the framboidal pyrite are rimmed by ore pyrite and/or the ore pyrite forms a matrix that partially fills the space between pyrite crystallites in the framboid, particularly in the rim area, resulting in the framboidal pyrite displaying a mixed geochemical signal of original diagenetic framboidal and ore-stage pyrites. The framboidal pyrite records the metallogenetic process. The S isotope characteristics of the framboidal pyrite rim also support the magmatic hydrothermal origin of the deposit. The findings confirm that the developed NanoSIMS method can be used for analyzing the δ^{34}S of pyrite samples with a limited analyzable region ($>1 \times 1$ μm^2).

Conclusions

We developed an *in situ* method for determining the sulfur isotope ratio (δ^{34}S) of microminerals with high spatial resolution (a square side of $\sim$1 μm) and precision (<0.5‰) by Nano-SIMS. These properties were achieved by improving the transmission and reducing the intensity of the primary beam. Four pyrite standard samples were analyzed to determine their sulfur isotope ratios using the developed method. The δ^{34}S of all the standard samples were consistent with previously recommended values with reproducibilities (1 SD) better than 0.5‰. EM aging and the height influence were shown to affect the accuracy of the high-resolution NanoSIMS sulfur analysis. The developed NanoSIMS method also allowed us to determine the S isotopic characteristics of the framboidal pyrite from the Shuiyingdong Carlin-type Au deposit. Our results indicate that the pyrite crystallite (<10 μm) comprising the framboidal pyrite is rimmed by ore pyrite, supporting the magmatic hydrothermal origin of the deposit. The developed NanoSIMS can be used for analyzing the δ^{34}S of samples with a limited analyzable region ($>1 \times 1$ μm^2) with high precision.

Author contributions

Youwei Chen and Jianfeng Gao conceived the presented idea. Jianfeng Gao supervised the project. Zhuojun Xie supplied the Shuiyingdong sample and contributed to the interpretation of the results. Shaohua Dong and Quanliang Lei assisted in the NanoSIMS and SEM analysis. Youwei Chen took the lead in writing the manuscript. All authors reviewed and edited the paper.

Conflicts of interest

There are no conflicts to declare.

Acknowledgements

References

1 H. Ohmoto, *Geochemistry of Hydrothermal Ore Deposits*, 1979, 509–567.

2 N. Grassineau, D. Mattey and D. Lowry, *Anal. Chem.*, 2001, **73**, 220–225.

3 D. E. Canfield, *Am. J. Sci.*, 2004, **304**, 839–861.

4 W. C. Shanks III, *Rev. Mineral. Geochem.*, 2001, **43**, 469–525.

5 P. R. Mason, J. Košler, J. C. De Hoog, P. J. Sylvester and S. Meffan-Main, *J. Anal. At. Spectrom.*, 2006, **21**, 177–186.

6 B. Rottier and A. Audétat, *Chem. Geol.*, 2019, **504**, 1–13.

7 J. De Hoog, P. Mason and M. m. van Bergen, *Geochim. Cosmochim. Acta*, 2001, **65**, 3147–3164.

8 Z. Bao, L. Chen, C. Zong, H. Yuan, K. Chen and M. Dai, *Int. J. Mass Spectrom.*, 2017, **421**, 255–262.

9 L. R. Riciputi, B. A. Paterson and R. L. Ripperdan, *Int. J. Mass Spectrom.*, 1998, **178**, 81–112.

10 J. Hammerli, N. D. Greber, L. Martin, A.-S. Bouvier, A. I. Kemp, M. L. Fiorentini, J. E. Spangenberg, Y. Ueno and U. Schaltegger, *Chem. Geol.*, 2021, **579**, 120242.

11 E. H. Hauri, D. Papineau, J. Wang and F. Hillion, *Chem. Geol.*, 2016, **420**, 148–161.

12 R. Kozdon, N. T. Kita, J. M. Huberty, J. H. Fournelle, C. A. Johnson and J. W. Valley, *Chem. Geol.*, 2010, **275**, 243–253.

13 N. T. Kita, J. M. Huberty, R. Kozdon, B. L. Beard and J. W. Valley, *Surf. Interface Anal.*, 2011, **43**, 427–431.

14 C. LaFlamme, L. Martin, H. Jeon, S. M. Reddy, V. Selvaraja, S. Caruso, T. H. Bui, M. P. Roberts, F. Voute, S. Hagemann, D. Wacey, S. Littman, B. Wing, M. Fiorentini and M. R. Kilburn, *Chem. Geol.*, 2016, **444**, 1–15.

15 M. Pimminger, M. Grasserbauer, E. Schroll and I. Cerny, *Anal. Chem.*, 1984, **56**, 407–411.

16 S. J. Mojzsis, C. D. Coath, J. P. Greenwood, K. D. McKeegan and T. M. Harrison, *Geochim. Cosmochim. Acta*, 2003, **67**, 1635–1658.

17 P. Hoppe, *Appl. Surf. Sci.*, 2006, **252**, 7102–7106.

18 M. L. Kraft, S. F. Fishel, C. G. Marxer, P. K. Weber, I. D. Hutcheon and S. G. Boxer, *Appl. Surf. Sci.*, 2006, **252**, 6950–6956.

19 T. Li, T. D. Wu, L. Mazéas, L. Toffin, J. L. Guerquin-Kern, G. Leblon and T. Bouchez, *Environ. Microbiol.*, 2008, **10**, 580–588.

20 D. McPhail, *J. Mater. Sci.*, 2006, **41**, 873–903.

21 J. Badro, F. J. Ryerson, P. K. Weber, A. Ricolleau, S. J. Fallon and I. D. Hutcheon, *Earth Planet. Sci. Lett.*, 2007, **262**, 543–551.

22 J. Yan, R. Hu, S. Liu, Y. Lin, J. Zhang and S. Fu, *Ore Geol. Rev.*, 2018, **92**, 29–41.

23 W. Wang, Y. Hu, A. D. Muscente, H. Cui, C. Guan, J. Hao and C. Zhou, *Geology*, 2021, **49**, 611–616.

24 S. L. Barker, K. A. Hickey, J. S. Cline, G. M. Dipple, M. R. Kilburn, J. R. Vaughan and A. A. Longo, *Econ. Geol.*, 2009, **104**, 897–904.

25 B. Winterholler, P. Hoppe, S. Foley and M. O. Andreae, *Int. J. Mass Spectrom.*, 2008, **272**, 63–77.

26 E. Harris, B. Sinha, P. Hoppe, J. Crowley, S. Ono and S. Foley, *Atmos. Chem. Phys.*, 2012, **12**, 407–423.

27 B. Sinha, P. Hoppe, J. Huth, S. Foley and M. Andreae, *Atmos. Chem. Phys.*, 2008, **8**, 7217–7238.

28 C. Floss, F. J. Stadermann, J. P. Bradley, S. Bajt, G. Graham and A. S. Lea, *Geochim. Cosmochim. Acta*, 2006, **70**, 2371–2399.

29 B. Winterholler, P. Hoppe, M. O. Andreae and S. Foley, *Appl. Surf. Sci.*, 2006, **252**, 7128–7131.

30 C. Floss, F. J. Stadermann, J. P. Bradley, Z. R. Dai, S. Bajt, G. Graham and A. S. Lea, *Geochim. Cosmochim. Acta*, 2006, **70**, 2371–2399.

31 J. Zhang, Y. Lin, W. Yang, W. Shen, J. Hao, S. Hu and M. Cao, *J. Anal. At. Spectrom.*, 2014, **29**, 1934–1943.

32 M. Nishizawa, S. Maruyama, T. Urabe, N. Takahata and Y. Sano, *Rapid Commun. Mass Spectrom.*, 2010, **24**, 1397–1404.

33 J. Zhang, Y. Lin, J. Yan, J. Li and W. Yang, *Anal. Methods*, 2017, **9**, 6653–6661.

34 D. E. Crowe and R. G. Vaughan, *Am. Mineral.*, 1996, **81**, 187–193.

35 J. Zhang, Doctor thesis, Institute of Geology and Geophysics, Chinese Academy of Sciences, 2015.

36 W. Yang, S. Hu, J. Zhang, J. Hao and Y. Lin, *Sci. China Earth Sci.*, 2015, **58**, 1758–1767.

37 M. R. Kilburn and D. Wacey, Nanoscale Secondary Ion Mass Spectrometry (NanoSIMS) as an Analytical Tool in the Geosciences, in *Principles and Practice of Analytical Techniques in Geosciences*, 2014, pp. 1–34.

38 J.-L. Hao, W. Yang, S. Hu, R.-y. Li, J.-L. Ji, H. G. Changela and Y.-T. Lin, *J. Anal. At. Spectrom.*, 2021, **36**, 1625–1633.

39 A. V. Walker, *Anal. Chem.*, 2008, **80**(23), 8865–8870.

40 T. R. Ireland, *Treatise on Geochemistry*, 2014, 385–409, DOI: **10.1016/b978-0-08-095975-7.01430-3**.

41 E. Zinner and G. Crozaz, *Int. J. Mass Spectrom. Ion Processes*, 1986, **69**, 17–38.

42 J. M. Hayes and D. A. Schoeller, *Anal. Chem.*, 1977, **49**, 306–311.

43 G. Slodzian, F. Hillion, F. J. Stadermann and E. Zinner, *Appl. Surf. Sci.*, 2004, **231–232**, 874–877.

44 G. Slodzian, *Appl. Surf. Sci.*, 2004, **231–232**, 3–12.

45 R. Ogliore, K. Nagashima, G. Huss and P. Haenecour, *Nucl. Instrum. Methods Phys. Res., Sect. B*, 2021, **491**, 17–28.

46 T. Ushikubo, K. H. Williford, J. Farquhar, D. T. Johnston, M. J. Van Kranendonk and J. W. Valley, *Chem. Geol.*, 2014, **383**, 86–99.

47 T. Ding, S. Valkiers, H. Kipphardt, P. De Bièvre, P. D. P. Taylor, R. Gonfiantini and R. Krouse, *Geochim. Cosmochim. Acta*, 2001, **65**, 2433–2437.

This journal is © The Royal Society of Chemistry 2022

J. Anal. At. Spectrom., 2022, **37**, 2529–2536 | **2535**

48 M. J. Whitehouse, *Geostand. Geoanal. Res.*, 2013, **37**, 19–33.

49 Z. Taracsák, D. A. Neave, P. Beaudry, J. Gunnarsson-Robin, R. Burgess, M. Edmonds, S. A. Halldórsson, M. A. Longpré, S. Ono, E. Ranta, A. Stefánsson, A. V. Turchyn, Eimf and M. E. Hartley, *Chem. Geol.*, 2021, **578**(120318).

50 G. Slodzian, M. Chaintreau, R. Dennebouy and A. Rousse, *Eur. Phys. J.: Appl. Phys.*, 2001, **14**, 199–231.

51 R. A. Stern, I. R. Fletcher, B. Rasmussen, N. J. McNaughton and B. J. Griffin, *Int. J. Mass Spectrom.*, 2005, **244**, 125–134.

52 Q.-L. Liang, Z. Xie, X.-Y. Song, R. Wirth, Y. Xia and J. Cline, *Econ. Geol.*, 2021, **116**, 515–526.

53 Z. Xie, Y. Xia, J. S. Cline, M. J. Pribil, A. Koenig, Q. Tan, D. Wei, Z. Wang and J. Yan, *Econ. Geol.*, 2018, **113**, 1627–1652.